Energy 103 (2016) 100–106

Contents lists available at ScienceDirect

Energy

journal homepage: www.elsevier.com/locate/energy

Hollow carbon sphere/metal oxide nanocomposites anodes for lithium-ion batteries

K. Wenelska [a, *, 1], A. Ottmann [b, 1], P. Schneider [b], E. Thauer [b], R. Klingeler [b, c], E. Mijowska [a]

[a] Institute of Chemical and Environment Engineering, West Pomeranian University of Technology, ul. Pulaskiego 10, 70-322, Szczecin, Poland
[b] Kirchhoff Institute of Physics, Heidelberg University, INF 227, 69120 Heidelberg, Germany
[c] Centre for Advanced Materials, Heidelberg University, INF 225, 69120 Heidelberg, Germany

ARTICLE INFO

Article history:
Received 20 August 2015
Received in revised form
26 December 2015
Accepted 9 February 2016

Keywords:
Lithium-ion batteries
Metal oxides
Nanoparticle
Hollow carbon spheres
Electrochemical properties

ABSTRACT

HCS (Hollow carbon spheres) covered with metal oxide nanoparticles (SnO_2 and MnO_2, respectively) were successfully synthesized and investigated regarding their potential as anode materials for lithium-ion batteries. Raman spectroscopy shows a high degree of graphitization for the HCS host structure. The mesoporous nature of the nanocomposites is confirmed by Brunauer–Emmett–Teller analysis. For both metal oxides under study, the metal oxide functionalization of HCS yields a significant increase of electrochemical performance. The charge capacity of HCS/SnO_2 is 370 mA hg^{-1} after 45 cycles (266 mA hg^{-1} in HCS/MnO_2) which clearly exceeds the value of 188 mA hg^{-1} in pristine HCS. Remarkably, the data imply excellent long term cycling stability after 100 cycles in both cases. The results hence show that mesoporous HCS/metal oxide nanocomposites enable exploiting the potential of metal oxide anode materials in Lithium-ion batteries by providing a HCS host structure which is both conductive and stable enough to accommodate big volume change effects.

1. Introduction

Rechargeable LIBs (Li-ion batteries) are currently the dominant energy storage technology for portable electronic devices. Despite their enormous commercial success in this field, for more demanding high power and high energy applications new materials have to be developed which enable significantly improved specific energy densities, capacities, and power rates in combination with long life time and cycling stability [1–3]. In case of the anodes, the most commonly used reference is graphite, which is a low-cost material with good cyclic stability but rather low electrochemical potential. Its limited reversible intercalation capacity (theoretically 372 mA hg^{-1}) and poor rate performance hinder its application in high-performance LIBs [4–6]. Accordingly, extensive efforts have been done to develop new high-performance anode materials for next-generation LIBs. One promising approach aims at utilizing redox-active metal oxides such as Fe_2O_3 [7], SnO_2 [8], and Co_3O_4 [9] which exhibit very high theoretical specific capacities as they are capable of converting up to 6 Li per formula unit [10–13]. Despite significant progress, however, metal oxide-based anodes do not yet reach their full potential which is mainly caused by their low conductivity and by large volume changes during dis-/charge cycling [14,15]. Hence, during electrochemical cycling, metal oxides typically break into small metal clusters, resulting in a large volume expansion and a loss of reversible capacity [16,17].

A materials-science based answer to these issues applies nanoscaled metal oxides embedded into conductive carbon structures. Such nanocomposites have indeed emerged as a promising method towards high-performance anode materials [18,19]. On the one hand, downscaling the active material yields short transport lengths for both, electrons and Li-ions, higher specific surface areas, and better accommodation of strain upon Li insertion/extraction [20,21]. To date, such composites are commonly prepared by simply coating pyrolytic carbon species on nanoscaled oxides [22,23]. However, while increasing the overall electronic conductivity of the materials, pyrolytic carbon does provide an effective host structure for accommodating the strain due to large volume expansion and such materials hence offer only limited cycling stability. Alternatively, creating composites with porous characteristics has been proposed to overcome these limitations [24–27]. Such composites can be achieved either by preparing hybrid composites or by producing nanostructured composites. Here, we report a facile

* Corresponding author.
E-mail addresses: kwenelska@zut.edu.pl (K. Wenelska), alex.ottmann@kip.uni-heidelberg.de (A. Ottmann).
[1] Both authors contributed equally to this work.

http://dx.doi.org/10.1016/j.energy.2016.02.063
0360-5442/

impregnation method [28] to synthesize HCS (hollow carbon spheres) covered with SnO_2 and MnO_2 nanoparticles as advanced anode material for high performance LIBs (see Fig. 1). The resulting nanocomposite materials displays reversible capacities larger than pristine HCS as well as good cycling performance.

2. Experimental section

Synthesis of solid SiO_2 nanospheres (SiO_2). SiO_2 spheres were prepared in a modified Stoeber process [29]. TEOS (Tetraethyl orthosilicate) (1.5 ml) was added to a mixture of ethanol (50 ml) and concentrated ammonia (28 wt%, 2.5 ml). Then the solution was stirred for 24 h. Afterwards, the product was separated by filtration, washed with ethanol and dried [30].

Synthesis of mesoporous silica spheres (SiO_2@m-SiO_2). In a typical synthesis, 100 mg of SiO_2 was dispersed in a solution containing CTAB (cetyltrimethylammonium bromide 0.8 g), deionized water, concentrated ammonia (28 wt%), and 60 ml ethanol. The suspension was sonicated and stirred for 60 min, then 1.43 ml of TEOS was added dropwise while stirring. The suspension was stirred for another 6 h, and afterwards, the product was filtered, washed with ethanol and water several times. Finally, the sample was dried in air at 100 °C for 24 h.

Carbonization of SiO_2@m-SiO_2 and removal of silica (HCS). The dried SiO_2@m-SiO_2_CTAB spheres were used as a template to prepare the hollow mesoporous carbon spheres using CVD (chemical vapor deposition). The silica spheres were placed in an alumina boat and put into a tube furnace. Argon and ethylene were introduced at a flow rate of 100 and 30 sccm, respectively. The temperature was raised to 800 °C, and the CVD reaction time was 3 h. Afterwards, the resulting SiO_2@m-SiO_2_C spheres were thoroughly washed with hydrofluoric acid to remove the silica components and finally hollow carbon spheres (HCS) were obtained.

Functionalization of HCS with metal oxide nanoparticles. Two samples of HCS modified by metal oxide nanoparticles (HCS/SnO_2 and HCS/MnO_2, respectively) were prepared according to the following procedure: 150 mg of HCS and 150 mg manganese acetonate (product referred to as HCS/MnO_2) or tin chloride (product referred to as HCS/SnO_2) were dispersed in 250 ml of ethanol and sonicated for 2 h. Afterwards, the mixture was stirred for another 24 h. Finally, the product was dried in air at 100 °C for 24 h.

Characterization. The morphology of the samples was investigated by a FEI Tecnai F30 TEM (transmission electron microscope) with a field emission gun operating at 200 kV and EDX (Energy-dispersive X-ray spectroscopy) as one mode. Powder XRD (X-ray diffraction) was performed on a Philips diffractometer using Cu-K_α radiation. Raman scattering was studied on a Renishaw micro-Raman spectrometer ($\lambda = 720$ nm). N_2 adsorption/desorption isotherms were acquired at liquid nitrogen temperature (77 K) using a Micromeritics ASAP 2010 M instrument, and the specific surface area was calculated by the BET (Brunauer Emmett Teller) method. TGA (Thermogravimetric analysis) was carried out on 10 mg samples using the DTA-Q600 SDT TA at a heating rate of 10 °C/min from room temperature to 900 °C in air flow (100 ml/min).

Electrochemical studies by means of cyclic voltammetry and galvanostatic cycling were carried out in Swagelok-type two-electrode cells by a VMP3 (Bio-Logic) potentiostat (see Ref. [30]). The working electrodes were prepared from a mixture of pristine material with carbon black (Super P, Timcal) and PVDF (polyvinylidene fluoride) binder (Solvay Plastics) in a weight ratio of 70:15:15. Additional carbon black was added in order to assure the mechanical stability of the electrodes. PVDF was dissolved in NMP (N-Methyl-2-pyrrolidon) and subsequently the active material and carbon black were mixed with the solution. The resulting slurry was pasted on circular copper plates and dried at 100 °C in a vacuum furnace (<5 mbar) over night. After mechanical pressing at 10 MPa, the electrodes were dried again. The Swagelok-type cells were assembled in an argon atmosphere glovebox (H_2O, $O_2 < 1$ ppm) with the working electrode, a lithium metal (Alfa Aesar) counter electrode, which had been pressed on a circular nickel plate, and two layers of glass microfibre separator (GF/D, Whatman). 200 μl of a 1 M solution of $LiPF_6$ in 1:1 EC (ethylene carbonate) and DMC (dimethyl carbonate) was used as electrolyte (LP30, Merck). While measuring, the cells were held at 25 °C in a climate chamber. For the CVs, the scan rate was fixed at 0.1 mV/s in the voltage range of 0.01–3.00 V and GCPL (Galvanostatic cycling with Potential Limitation) measurements were done at current densities of 100–1000 mA h/g.

3. Results and discussion

Fig. 2 shows TEM images of pristine hollow carbon spheres and of HCS/metal oxide composites with different metal oxide loading. As observed in Fig. 2(a,b), the pristine HCS are uniform in diameter which amounts about 250 nm. The shell thickness is about 90 nm. Functionalization with SnO_2 nanoparticles yields HCS/SnO_2 with a small metal oxide particle size distribution ranging from 3 to 5 nm. The particle sizes have been derived from averaging over 100 nanoparticles observed in the TEM image (Fig. 2(c,d)). SnO_2 nanoparticles are distributed on the surface of HCS homogeneously. Similar results are obtained for HCS/MnO_2 (Fig. 2(e, f)). However, the diameter of MnO_2 nanoparticles is smaller, ranging from 1 to 3 nm. As shown in Fig. 3, EDX elemental mapping clearly reveals that the elements Sn, O, and C are evenly distributed throughout the HCS/SnO_2 nanocomposite. Similarly, the elemental mappings of HCS/MnO_2 indicate the presence of Mn, O, and C. All detected elements seem to be rather homogeneously distributed in the sample. In summary, the EDS data clearly show that SnO_2 and MnO_2 are located both in the core and the shell of the hollow carbon spheres.

The carbon content and the quality of the materials are evaluated by TGA (thermogravimetric analysis) (Fig. 4) and Raman spectroscopy (Fig. 5). The thermogravimetric analyses of the HCS, HCS/SnO_2, and HCS/MnO_2 samples present the thermal stability by monitoring the change of weight during heating. From the TGA results (Fig. 4), the pristine HCS start to oxidize around 550 °C [31]. The HCS are completely exhausted when the temperature is increased to ~700 °C in air, which indicates high purity of the HCS. TGA measurements for HCS with metal oxide nanoparticles show ash contents of 24 wt% and 37 wt% for MnO_2 and SnO_2, respectively. In comparison to the pristine HCS, the stabilities of both metal

Fig. 1. Synthesis schematic of hollow carbon spheres (black) decorated with metal oxide nanoparticles (blue). Mesoporous silica spheres (grey) are being carbonized (step 2). After removal of silica (step 3), the resulting hollow carbon sphere is functionalized by metal oxide nanoparticles (step 4). (See the text.) (For interpretation of the references to colour in this figure legend, the reader is referred to the web version of this article.)

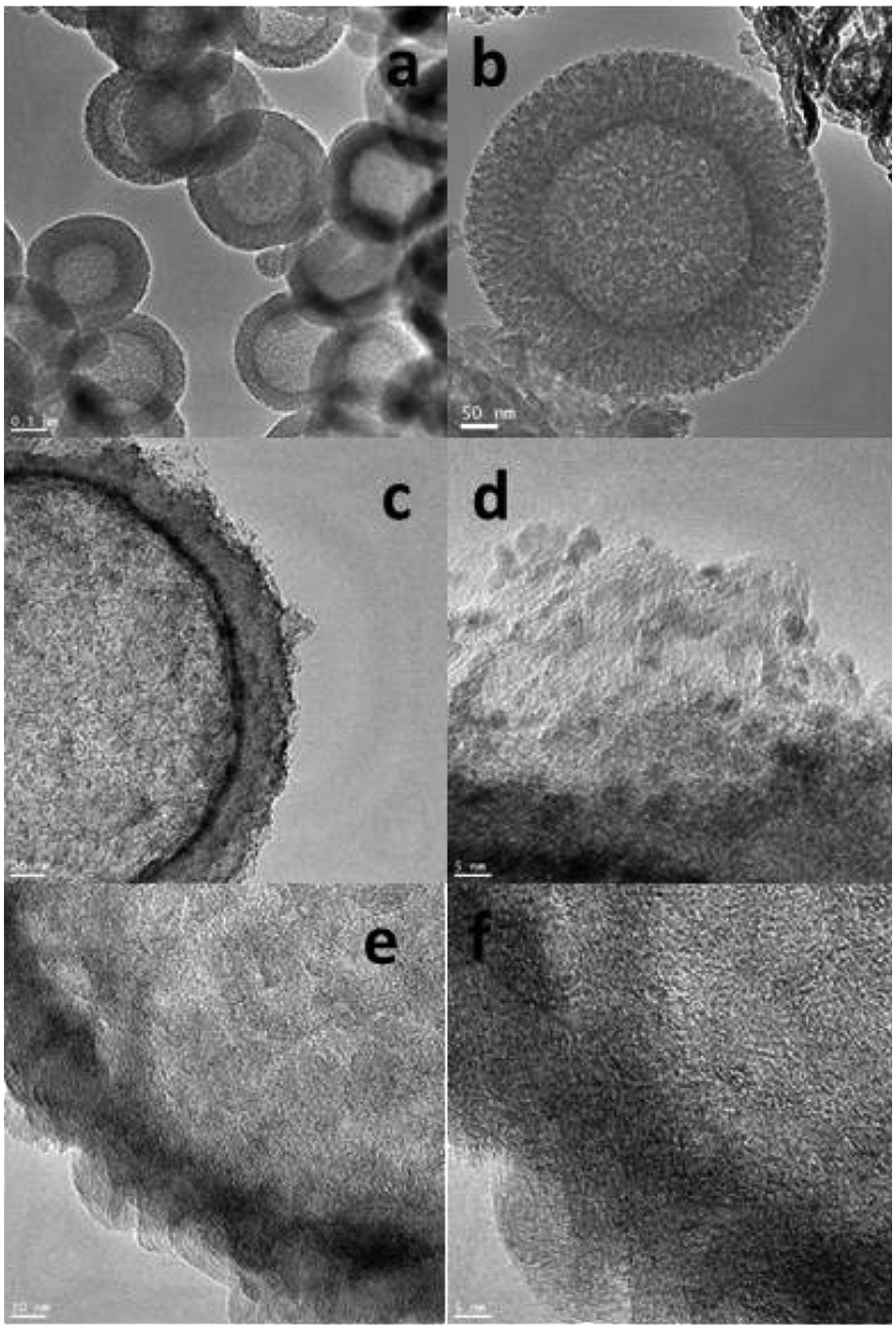

Fig. 2. TEM images of hollow carbon spheres (a, b), HCS/SnO_2 (c,d), HCS/MnO_2 (e,f).

oxide-functionalized HCS materials are weaker. The main weight loss starts at around 400 °C for both HCS/metal oxide materials. One may conclude that the interaction of the metal oxides and the carbon induces lower stability of HCS. Additionally, a mass loss of ~10% is observed in the thermal profile of HCS/MnO_2 starting at ~210 °C. This feature presumably originates from the decomposition of residual manganese acetate.

In the Raman spectra, two obvious peaks are detected around 1314 and 1595 cm^{-1}, which correspond to disordered carbon (D) and ordered graphitic carbon (G), respectively, as shown in Fig. 5. In case of the pristine HCS, the I_G/I_D intensity ratio of the G- and D-lines amounts to 0.9, indicating a high degree of graphitization. Note, that such a high crystallinity in general supports high electrical conductivity as desirable for application in Li-ion electrodes. Upon deposition of the metal oxide nanoparticles, the relation of G-to D-band intensities slightly decreases which is consistent with the assumption that additional defects are formed in the HCS structures. The D-mode is most pronounced for HCS/MnO_2, indicating the highest concentration of defects and hence the lowest stability as it is experimentally observed in the TGA data.

The XRD patterns of the synthesized samples confirm the presence of graphitic carbon and metal oxides in the functionalized materials (Fig. 6). For pristine HCS, there are two broad peaks at 24.9° and 42° which can be ascribed to graphitic carbon. In addition to the carbon peaks, HCS/metal oxides exhibit further diffraction peaks. In HCS/SnO_2, there are major peaks at 33.9°, 51.8°, and 65.8°,

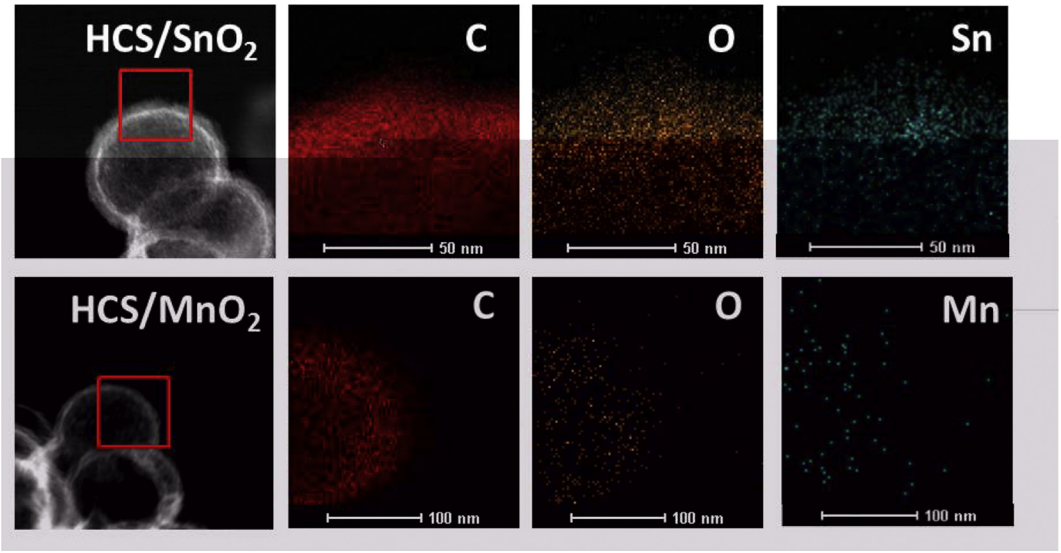

Fig. 3. EDS mapping of HCS/SnO_2 and HCS/MnO_2. (See the text.)

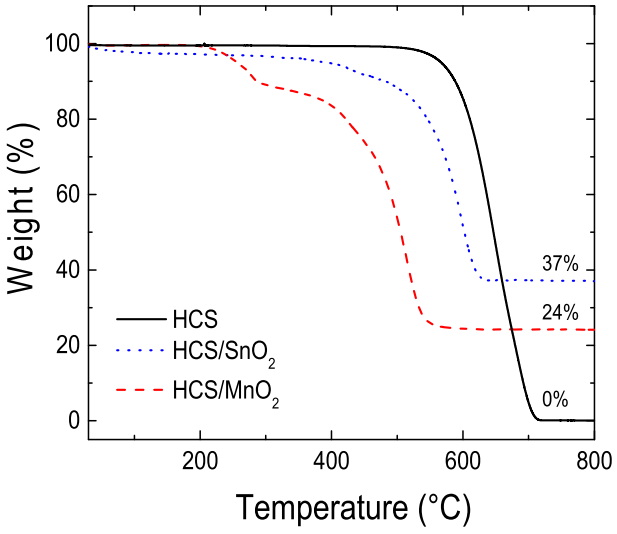

Fig. 4. TGA profiles of HCS, HCS/SnO_2, and HCS/MnO_2.

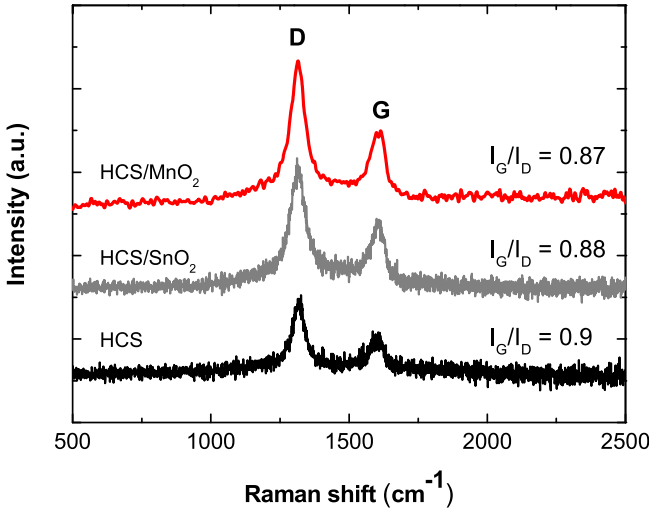

Fig. 5. Raman spectra of HCS, HCS/SnO_2, and HCS/MnO_2.

which can be attributed to tetragonal SnO_2 nanomaterials. The XRD pattern of HCS/MnO_2 shows characteristic peaks for β-MnO_2 at $2\Theta = 27°, 54°, 56°, 68.7°$ [32].

The BET (Brunauer–Emmett–Teller) specific surface area and the porosity of all samples studied by nitrogen adsorption–desorption analysis confirms the mesoporous nature of the materials (Fig. 7(a)). The data show a typical type II behaviour with a H1 hysteresis loop, indicating a disordered mesoporous structure [33] Quantitatively, the BET specific surface area of pristine HCS amounts to 652 m^2/g. It significantly drops for the metal oxide covered nanospheres to 302 m^2/g for HCS/SnO_2 and 184 m^2/g for HCS/MnO_2. The corresponding mesopore size distribution in HCS calculated by means of the BET method from the adsorption branch reveals non-uniform pores centered at approximately 3.6, 6.0, and 12.7 nm. In HCS/SnO_2, the pores sizes are 3.3, 4.1 and 6.7 nm, and in HCS/MnO_2 they are centered at 3.7, 4.7, 6.1, 8.4 and 21 nm. The observation of smallest pore volume and surface area in HCS/MnO_2 suggests that the MnO_2 nanoparticles block the pore of the hollow carbon spheres in this case. The pore size distributions shown in Fig. 7(b) demonstrate the presence of bimodal porosity: there are mesopores and macropores. Such porous structures, e.g., allow easy access of Li^+ ions to the active materials and are hence enhancing diffusion kinetics [34,35].

3.1. Electrochemical properties

The CV (cyclic voltammograms) in Fig. 8 show the characteristics of the electrochemical processes upon variation of the potential with 0.1 mV/s in the range between 0.01 and 3.0 V. For HCS, several well-known features in carbon structures are observed. The first cycle, starting with a negative voltage ramp at 3.1 V, shows reduction peaks at 0.01 V, 0.6 V and 1.35 V. Oxidation occurs at 0.2 V, around 1.2 V, and above 2 V. The reduction peak at 0.6 V can be attributed to the formation of a passivating SEI (solid electrolyte interface) on the carbon surfaces [36]. Correspondingly, this peak disappears upon further cycling but in the overall behaviour a shoulder shows up around 0.8 V (see Fig. 8(b)). It might indicate an ongoing irreversible contribution from the SEI formation or might be related to the oxidation process at 1.2 V which decreases upon

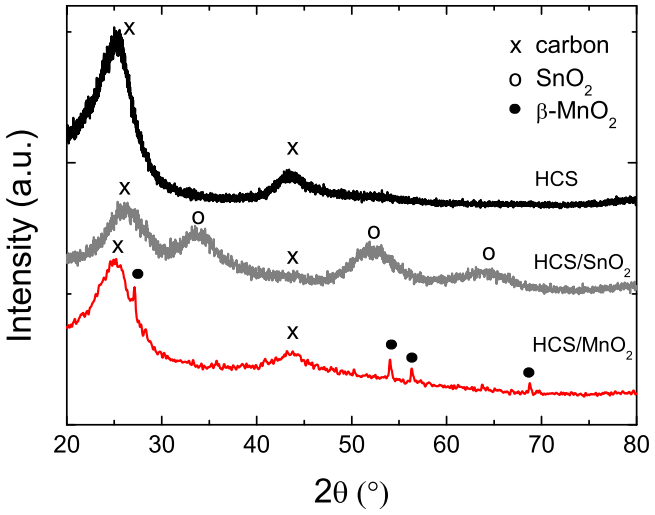

Fig. 6. XRD spectra of HCS, HCS/SnO_2, and HCS/MnO_2. The crosses, open and filled cycles label diffraction peaks associated with graphitic carbon, SnO_2, and β-MnO_2, respectively.

Functionalization of HCS by means of SnO_2 and MnO_2 nanoparticles yields additional features in the CVs. In cycle 1 (Fig. 8(a)), initial reduction processes of SnO_2 and MnO_2 to corresponding metals and formation of amorphous Li_2O shows up. In the case of HCS/SnO_2, in addition to the processes for HCS discussed above, there are reduction peaks at 0.97 V, 0.69 V, 0.42 V, and 0.07 V, while additional/more pronounced oxidations are observed around 0.53 V and 1.23 V (the latter being much more pronounced than in HCS) in the 1st cycle. Upon further cycling, the three reduction peaks at 0.97 V, 0.69 V, and 0.42 V merge to a plateau-like shoulder.

According to [33,34] the electrochemical behaviour of SnO_2 can be described via

$$4Li^+ + SnO_2 + 4e^- \Delta Sn + 2Li_2O \quad (1)$$

$$xLi^+ + Sn + xe^- \Delta Li_xSn (0 \le x \le 4.4) \quad (2)$$

The redox pair at 0.07 V/0.53 V can be attributed to the reversible alloying and dealloying of Sn and Li (reaction 2) [38]. The reduction peak at 0.42 V might also be part of this alloying process [39]. The reduction peaks at 0.69 V and 0.97 V in the first cycle

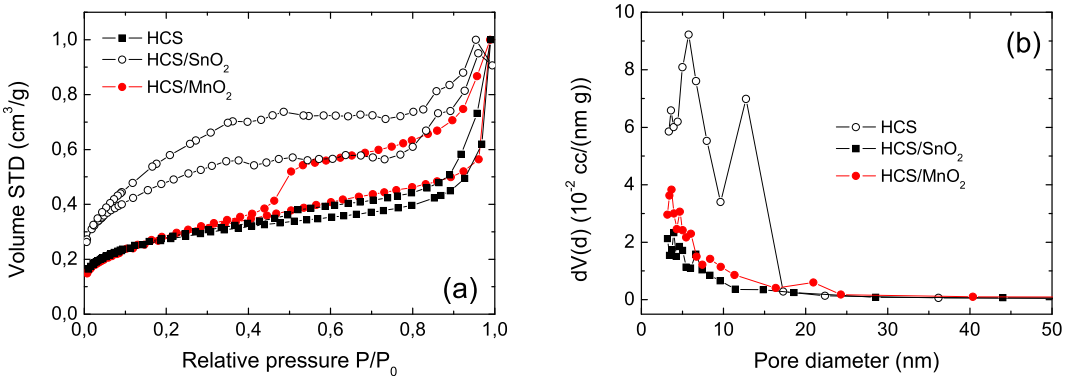

Fig. 7. (a) N_2 adsorption/desorption isotherms and (b) pore size distribution profile for HCS, HCS/SnO_2, and HCS/MnO_2.

cycling as well. In contrast, the red./ox. pair at 0.01/0.2 V corresponds to reversible de-/intercalation of Li-ions into the carbon structures. With increasing cycle number the peak height of the reduction peak decreases while the oxidation peak intensity increases and shifts to slightly lower potentials. The origin of the reduction peak appearing at 1.35 V in the first cycle only is unknown. The oxidative contributions above 2 V are presumingly originating from the cell setup.

The evolution of the dis-/charge capacities in HCS (Fig. 9) upon cycling is typical for carbon structures. In the initial charge/discharge process performed at 100 mA/g the material shows capacities of 1305 mA h/g and 269 mA h/g, respectively. The next cycles show a huge drop-off mainly due to the absence of the irreversible contribution of SEI formation in the first cycle. Quantitatively, the discharge capacity amounts to 190 mA h/g after 10 cycles. This is clearly below the theoretical capacity of 372 mA h/g. We associate this observation to the presence of amorphous carbon as indicated by the Raman and the XRD data (Figs. 5 and 6) which implies lower capacities as compared to graphite [37]. Increasing the charge/discharge current to 250, 500 and 1000 mA/g yields 153/149 mA h/g (after 20 cycles), 124/123 mA h/g (30 cycles), and 103/103 mA h/g (40 cycles). In cycle 45, back at 100 mA/g, the charge and discharge capacities are 188 mA h/g and 179 mA h/g, respectively, which is more than 90% of the capacities reached in the 10th cycle.

presumingly correspond to the reduction of SnO_2 to Sn + Li_2O (reaction 1) and to the SEI formation [40–42]. The corresponding oxidation of Sn is supposed to appear around 1.2 V, i.e. this process superimposes another oxidation peak around 1.2 V which is also present in the case of pristine HCS. It is worth mentioning that the specific peak current in the voltage range of SEI formation is just ~200 mA/g compared to ~500 mA/g for HCS. We attribute this diminishment to SnO_2 nanoparticles on the HCS surface which alter the surface area and the chemistry of the interface to the electrolyte.

The presence of SnO_2 nanoparticles enables alloying of Sn (reaction 2), thereby increasing the capacity of pure HCS. Indeed, the charge/discharge capacities (370 mA h/g and 364 mA h/g) in the 45th cycle are much higher than the respective values of pure HCS (188 mA h/g and 179 mA h/g). Quantitatively, the experimental values are slightly lower than if the full theoretical capacity of the completely reversible process (2) is considered. A maximum value of x = 4.4 corresponds to a theoretical capacity of 783 mA h/g. Considering the mass fraction of SnO_2 being 37% (and 63% of HCS with 179 mA h/g in cycle no. 45), a completely reversible process would result in a specific discharge capacity of 402 mA h/g. The observed value of 364 mA h/g hence would indicate x ~4.0 in cycle no. 45, i.e. only rather small irreversibility. We note, however, that the SnO_2 coating also may diminish the available capacity of HCS as compared to the pure reference material due to blocking of pores

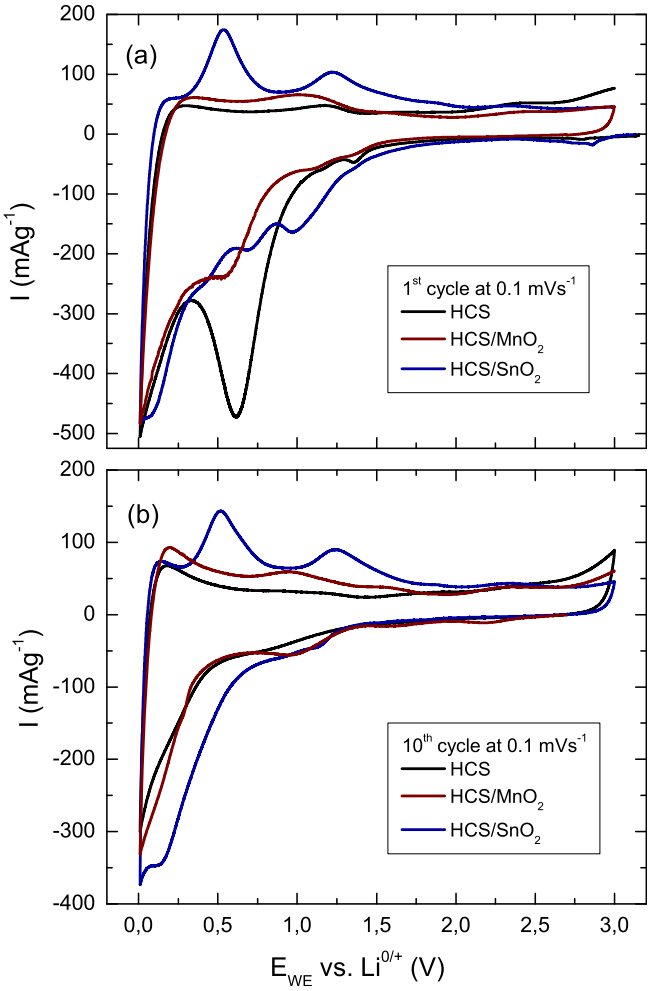

Fig. 8. Cyclic voltamograms of HCS, HCS/SnO_2, and HCS/MnO_2, obtained at a scan rate of 0.1 mV/s (a) shows the 1st cycle, (b) the 10th cycle.

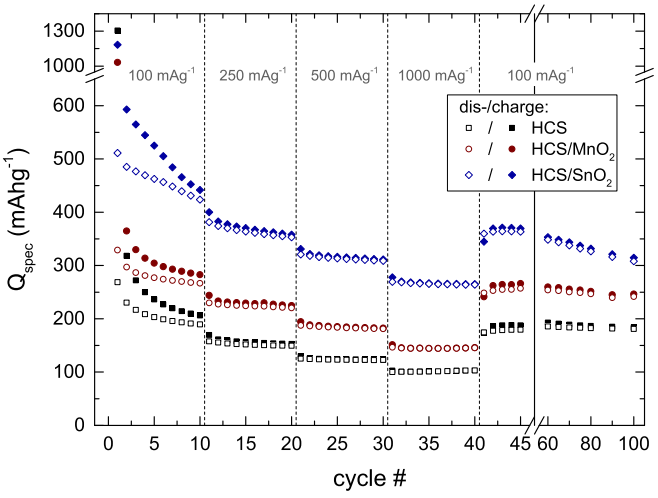

Fig. 9. Gravimetric specific capacities vs. cycle number of HCS, HCS/SnO_2, and HCS/MnO_2, at different scan rates.

for instance, which is indicated by a lower specific surface area of the HCS/SnO_2 composite (Fig. 7). We emphasize that rather large charge/discharge capacities of 315/308 mA h/g are still achieved after 100 cycles and therefore, 85% of the charge/discharge capacity is maintained over 55 cycles at 100 mA/g (from 45th to 100th).

Since HCS/MnO_2 exhibits a lower fraction of MnO_2, the effect of metal oxide functionalization is less pronounced than in HCS/SnO_2. The conversion reaction is however visible in the CVs in Fig. 8 as demonstrated by the broad oxidation peak around 1 V and a reductive feature around 0.35 V, which is overlain in the 1st cycle and hardly visible in subsequent ones. This redox pair is associated to the following reaction [43,44]:

$$MnO_2 + 4Li^+ + 4e^- \Delta 2LiO_2 + Mn \quad (3)$$

Comparing the peak current of the SEI formation in HCS and HCS/MnO_2, i.e. 500 mA/g and 250 mA/g, respectively, illustrates lower activity of the functionalized material. Qualitatively, this corresponds to the same effect as in the case of HCS/SnO2, namely a significantly reduced surface area of nearly 4 times less, i.e. a reduced interfacial area of carbon to the electrolyte.

The charge/discharge capacity in the 45th cycle is 266/257 mA h/g compared to 188/179 mA h/g for HCS. We conclude that the present MnO_2 mass fraction of 24% is associated to a discharge capacity of 121 mA h/g which is less than half of the theoretical value of 296 mA h/g^{-1} (0.24 * 1233 mA h/g). A likely reason for the inferior efficiency compared to the HCS/SnO_2 sample is the smaller specific surface area (184 vs. 302 m^2/g) due to in average much larger MnO_2 nanoparticles which might e.g. hinder efficient Li^+ transport. Furthermore, residual precursor (manganese acetate) in the material, as indicated by TGA results (Fig. 4), would also have a considerably negative impact on the electrochemical performance because it is electrochemically inactive. Nevertheless, a capacity retention of more than 90% over 55 cycles (from 45th to 100th) at 100 mA/g is observed. This cyclic stability (similar for HCS/SnO_2) argues for the benefit of utilizing HCS in order to maximize the potential of metal oxide anode materials by strain accommodation and by providing a conductive network.

4. Conclusions

The present work hence reveals advantages of the lithium storage in HCS/metal oxide materials providing a route to develop high-performance mesoporous hybrid materials. Considering that metal oxides are cost-effective and a potential large-scale production of HCS, the synthesized materials hold great potential for real applications. This effective strategy can be easily expanded to construct other high-performance architectures of functionalized HCS with other metal oxides, providing a general and effective approach towards high-performance metal-oxide-based anodes. In addition, the synthetic route developed in this work is facile and easily extendable to other Li-storable metals or alloys for the development of advanced anode materials of Li-ion batteries.

Acknowledgments

The authors are grateful for financial support of German Academic Exchange Service DAAD (PPP project no. 56269175) and the National Science Centre PRELUDIUM 6 UMO-2013/11/N/ST8/00651.

References

[1] Liu J, Cao G, Yang Z, Wang D, Dubois D, Zhou X, et al. Oriented nanostructures for energy conversion and storage. Chem Sus Chem 2008;1:676–97.
[2] Bruce PG, Scrosati B, Tarascon JM. Nanomaterials for rechargeable lithium batteries. Angew Chem Int Ed 2008;47:2930–46.
[3] Amjad S, Rudramoorthy R, Neelakrishnan S, Sri Raja Varman K, Arjunan TV. Evaluation of energy requirements for all-electric range of plug-in hybrid electric two-wheeler. Energy 2011;36(3):1623–9.

[4] Ban C, Wu Z, Gillaspie DT, Chen L, Yan Y, Blackburn JL, et al. Nanostructured Fe_3O_4/SWNT electrode: binder-free and high-rate Li-ion anode. Adv Mater 2010;22:145–9.
[5] Yang Z, Meng Q, Guo Z, Yu X, Yu X, Guo T, et al. Highly reversible lithium storage in uniform $Li_4Ti_5O_{12}$/carbon hybrid nanowebs as anode material for lithium-ion batteries. Energy 2013;55:925–32.
[6] Pang H, Yang Z, Lv J, Yang W, Guo T. Novel MnOx@carbon hybrid nanowires with core/shell architecture as highly reversible anode materials for lithium ion batteries. Energy 2014;69:392–8.
[7] Ke F-S, Huang L, Solomon BC, Wei GZ, Xue L-J, Zhang B, et al. Three-dimensional nano-architecture of Sn-Sb-Co Alloy as an anode of lithium-ion batteries with excellent lithium storage performance. J Mater. Chem 2012;22:17511–7.
[8] Jia X, Chen Z, Cui X, Peng Y, Wang X, Wang G, et al. Building robust architectures of carbon and metal oxide nanocrystals toward high-performance anodes for lithium-ion batteries. ACS Nano 2012;6:9911–9.
[9] Zhang HX, Feng C, Zhai YC, Jiang KL, Li QQ, Fan SS. Cross-stacked carbon nanotube sheets uniformly loaded with SnO_2 nanoparticles: a novel binder-free and high-capacity anode material for lithium-ion batteries. Adv Mater 2009;21:2299–304.
[10] Wang Z, Zhou L. Metal oxide hollow nanostructures for lithium-ion Batteries. Adv Mater 2012;24:1903–11.
[11] Liu XM, Zhang B, Ma PC, Yuen MM, Kim J-K. Carbon nanotube (CNT)-based composites as electrode material for rechargeable Li-ion batteries: a review. Compos Sci Technol 2012;72:121–44.
[12] Mao S, Wen Z, Kim H, Lu G, Hurley P, Chen J. A general approach to one-pot fabrication of crumpled graphene-based nanohybrids for energy applications. ACS Nano 2012;6:7505–13.
[13] Latorre-Sanchez M, Primo A, Garcia H. Green synthesis of Fe_3O_4 nanoparticles embedded in a porous carbon matrix and its use as anode material in Li-ion Batteries. J Mater. Chem 2012;22:21373–5.
[14] Muraliganth T, Murugan AV, Manthiram A. Facile synthesis of carbon-decorated single-crystalline Fe_3O_4 nanowires and their application as high performance anode in lithium ion batteries. Chem Commun 2009:7360–2.
[15] Rui X, Fengchun S, Hongwen H, Trong Duy N. A data-driven adaptive state of charge and power capability joint estimator of lithium-ion polymer battery used in electric vehicles. Energy 2013;63(0):295–308.
[16] Jia X, Chen Z, Suwarnasarn A, Rice L, Wang X, Sohn H, et al. High-performance flexible Lithium-ion electrodes based on robust network architecture. Energy Environ Sci 2012;5:6845–9.
[17] Fengchun S, Xiaosong H, Yuan Z, Siguang L. Adaptive unscented Kalman filtering for state of charge estimation of a lithium-ion battery for electric vehicles. Energy 2011;36(5):3531–4.
[18] Wang H, Liang Y, Gong M, Li Y, Chang W, Mefford T, et al. An ultrafast nickel–iron battery from strongly coupled inorganic nanoparticle/nanocarbon hybrid materials. Nat Commun 2012;3:917.
[19] Zhang H, Yu X, Braun PV. Three-dimensional bicontinuous ultrafast-charge and discharge bulk battery electrodes. Nat Nano-technol 2011;6:277–81.
[20] Zhu X, Ning G, Ma X, Fan Z, Xu C, Gao J, et al. High density Co_3O_4 nanoparticles confined in a porous graphene nanomesh network driven by an electrochemical process: ultra-high capacity and rate performance for lithium ion batteries. J Mater. Chem A 2013;1:14023–30.
[21] Tarascon JM, Armand M. Issues and challenges facing rechargeable lithium batteries. Nature 2001;41:359–67.
[22] Wang S, Ren Y, Liu G, Xing Y, Zhang S. Peanut-like MnO@ C core –shell composites as anode electrodes for high-Performance lithium ion batteries. Nanoscale 2013;6:3508–12.
[23] Goodenough JB, Park KS. The Li-ion rechargeable battery: a perspective. J Am Chem Soc 2013;135:1167–76.
[24] Xing Y, Wang Y, Zhou C, Zhang S, Fang B. Simple synthesis of mesoporous carbon nanofibers with hierarchical nanostructure for ultrahigh lithium storage. ACS Appl Mater. Interfaces 2014;6:2561–7.
[25] Wu HB, Chen JS, Hng HH, Lou XW. Nanostructured metal oxide-based materials as advanced anodes for lithium-ion batteries. Nanoscale 2012;4:2526–42.
[26] Liu C, Li F, Ma L, Cheng H. Advanced materials for energy storage. Adv Mater 2010;22:E28–62.
[27] Reddy MV, Subba Rao GV, Chowdari BVR. Metal oxides and oxysalts as anode materials for Li ion batteries. Chem Rev 2013;113:5364–457.
[28] Zhang K, Han P, Gu L, Zhang L, Liu Z, Kong Q, et al. Synthesis of nitrogen-doped MnO/Graphene nanosheets hybrid material for lithium ion batteries. ACS Appl Mater. Interfaces 2012;4:658–64.
[29] Stoeber W. J Colloid Interface Sci 1968;26:62–9.
[30] Neef C, Jähne C, Meyer HP, Klingeler R. Hydrothermal synthesis of flower-like $LiMnPO_4$ nanostructures self-assembled with (010) nanosheets and their application in Li-ion batteries. Langmuir 2013;29:8054–60.
[31] Chen X, Kierzek K, Jiang Z, Chen H, Tang T, Wojtoniszak M, et al. Synthesis, growth mechanism, and electrochemical properties of hollow mesoporous carbon spheres with controlled diameter. J Phys Chem C 2011;115:17717–24.
[32] Patterson AL. The Scherrer formula for X-ray particle size determination. Phys Rev Lett 1939;56:978–82.
[33] Zhang J, Wang K, Xu Q, Zhou Y, Cheng F, Guo S. Beyond yolkshell nanoparticles: Fe_3O_4@Fe_3C Core@Shell nanoparticles as yolks and carbon nanospindles as shells for efficient lithium ion storage. ACS Nano 2015;9(3):3369–76.
[34] Ji LW, Lin Z, Guo BK, Medford A, Zhang J. Electrospun materials for lithium and sodium rechargeable batteries: from structure evolution to electrochemical performance. Chem Eur J 2010:11543–8.
[35] Wen Z, Wang Q, Zhang Q, Li J. In situ growth of mesoporous SnO_2 on multiwalled carbon nanotubes: a novel composite with porous-tube structure as anode for lithium batteries. Adv Funct Mater 2007;7:2772.
[36] Novák P, Joho F, Lanz M, Rykart B, Panitz JC, Alliata D, et al. The complex electrochemistry of graphite electrodes in lithium-ion batteries. J Power Sources 2001:39–46.
[37] Winter M, Besenhard JO, Spahr ME, Novák P. Insertion electrode materials for rechargeable lithium batteries. Adv Mat 1998;10:725–63.
[38] Lou XW, Chen JS, Chen P, Archer LA, et al. One-pot synthesis of carbon-coated SnO_2 nanocolloids with improved reversible lithium storage properties. Chem Mat 2009;21:2868–74.
[39] Courtney IA, Dahn JR. Electrochemical and in situ X-ray diffraction studies of the reaction of lithium with tin oxide composites. Electrochem Soc 1997;144(6):2045–52.
[40] Li X, Li X, Zhang J, Liao Ch, Li X, et al. The carbon nanotube fibers for optoelectric conversion and energy storage. Mater Lett 2014;130:232–5.
[41] Thomas R, Mohan G. Phase and dimensionality of tin oxide at graphene nanosheet array and its electrochemical performance as anode for lithium ion battery. Electrochimica Acta 2014;125:380–5.
[42] Graphene wrapped $Sn_xTi_{1-x}O_2$ nanoparticles as an anode material for Li-ion batteries. Adv Mater 2009;21:2536–9.
[43] Wu MS, Julia Chiang P, Lee J, Lin J, et al. Synthesis of manganese oxide electrodes with interconnected nanowire structure as an anode material for rechargeable lithium ion batteries. J Phys Chem B 2005:10923279–84.
[44] Poizot P, Laruelle S, Grugeon S, Dupont L, Tarascon JM. Nano-sized transition-metal oxides as negative-electrode materials for lithium-ion batteries. Nature 2000:496.